UO_2 microstructural evolutions induced by Ni, Mo, and W dopants for intentional forensics

Denise Adorno Lopes,[1] Tash Ulrich, [1] Andrew Kercher, [1] Michael Bronikowski,[2] Kyle Samperton, [2] Spencer Scott, [2] Matthew Wellons, [2] Gage Green, [2] Tyler Spano, [1] Jason Harp, [1] Andrew Nelson, [1] and Ashley Shields[1]

1. Oak Ridge National Laboratory, 1 Bethel Valley Road, Oak Ridge, TN 37830

2. Savannah River National Laboratory, Aiken, SC, 29808

Corresponding author: adornolopesd@ornl.gov

Abstract

The concept of tagging nuclear fuel with a chemical barcode to enable forensics analysis across the nuclear fuel cycle is an area of active investigation, particularly to ensure fabrication viability without disrupting current fuel performance. This study explored the feasibility of using Ni, Mo, and W isotopic double-spikes as dopants in UO_2 fuel from the perspective of fuel fabrication. Doped UO_2 pellets were produced using conventional fuel fabrication processes, including powder mixing, sieving, pressing, and sintering in a reductive atmosphere. Two composition levels, 100 and 1000 ppm, were evaluated for each dopant element with isotopic double-spike configurations. For the Ni system, additional dopant concentrations of 250 and 500 ppm were produced with nonperturbed isotopic ratios. The results demonstrated that successful incorporation of Ni, Mo, and W double-spikes into UO_2 pellets occurred with minimal shift in final density or dopant loss during pellet fabrication. Isotopic analysis confirmed the presence of the double-spike signature even when diluted with natural isotopic material in ratio of 1:5 in the fabrication process. Microstructural examinations revealed different impacts on grain size compared with undoped UO_2. This study showed that Ni incorporation up to ~500 ppm promoted moderate grain growth, whereas the Mo and W systems caused grain size reduction at all concentrations. Changes in the UO_2 lattice parameter as a function of composition were detected exclusively for Ni up to 500 ppm, indicating that the Ni solid solution was the main factor for the observed grain growth. Insoluble (Mo and W) or supersaturated (Ni > 500 ppm) conditions produced grain size reduction. The Ni-doped pellets in the solution range resulted in a final microstructure within fuel specifications, demonstrating its potential benefits of employing complex dopant systems for potential nuclear forensic applications.

Abbreviations: CRM, certified reference material; FGR, fission gas release; FIMA, fissions per initial metal atom; HFIR, High Flux Isotope Reactor; ICP, inductively coupled plasma; MS, mass spectrometry; OES, optical emission spectroscopy; SEM, scanning electron microscope; XRD, x-ray diffraction

1 Introduction

The emerging concept of intentional nuclear forensics is gaining interest among stakeholders, particularly with the anticipated growth of advanced and modular nuclear reactor types and the consequent expansion of the nuclear supply chain [1]. This concept involves creating a chemical signature, or *barcode*, through the addition of dopants, also called *taggants*, enabling the fuel material's origins to be identified from fabrication to reprocessing and final storage [2-4] [5] [6]. This capability could theoretically support both the integrity of nuclear materials and the provenance assessment of materials found outside of regulatory control.

Previous research has identified potential taggant elements based on criteria such as detectability, ease of fabrication, and neutron absorption properties, especially when considering *double-spike* isotopes (i.e., isotopic pairs deliberately enriched and used to create a unique isotopic signature for tracing) [7]. Elements such as Fe, Ni, Mo, W, and others have been proposed for oxide fuel types, with Al, V, Nb, and Ta potentially being more suitable for metallic fuel types [8] [9] [10]. These elements were selected owing to the likelihood that they will provide unique signatures that can be predicted throughout stages of the nuclear fuel cycle, aiding in the identification of nuclear materials in a forensics investigation.

To date, the bulk of literature reports in this area have centered on the research and development of primary forensic assessments outlined in the previous paragraph. Work remains to evaluate the effect of potential taggant species on fuel fabrication, fresh fuel microstructure, unirradiated fuel properties, and, most critically, potential effects on fuel performance. Each of these areas are essential for determining the most effective methods for adding taggants to nuclear fuel; ensuring their stability, detectability, and compatibility with existing fabrication processes; and avoiding detrimental effects on reactor performance, safety, or fuel cycle economics. An assessment of taggants with respect to these criteria will directly contribute to consolidation, refinement, or expansion of the list of candidate taggants.

The incorporation of taggants into nuclear fuel would ideally adhere to two main considerations:

> (1) No major changes to the fuel fabrication process should be necessary. Obtaining a license for a nuclear fuel production facility is a time- and resource-intensive endeavor, with strict requirements related to fuel composition, uranium-235 (^{235}U) enrichment levels, and allowable concentrations of impurities (foreign elements). The difficulty of securing such licenses is underscored by the limited number of commercial fuel manufacturing facilities currently operating in the United States (e.g., Westinghouse in Columbia, Framatome in Richland, Global Nuclear Fuel in Wilmington, and BWX Technologies in Lynchburg) [11], as well as globally [12].

(2) The incorporation of taggants should not alter fuel specifications that dictate performance and are cited in regulatory licenses [13]. Fuel specifications typically include parameters such as pellet density, grain size, composition, impurity levels, geometry with tolerances (for a specific reactor design). Additionally, fuel licenses must be obtained individually in each country within its respective regulatory framework [14]. Introducing elements that alter the fuel specifications could require requalification across countries where power plants already use UO_2 fuel. Thus, an intentional forensics taggant strategy that minimizes changes to the specifications of actively-licensed UO_2 fuel is desirable.

Commercial light-water reactors using UO_2 fuel make up the majority of the global nuclear fuel capacity, making the evaluation of forensic technologies for this platform a logical focus. Nuclear fuel vendors are, to some extent, comfortable with the use of additives or dopants in UO_2. The industry has long evaluated a range chemical additives to enhance sintering, normalize microstructure, or encourage grain growth [15] [16] [17] [18] [19] [20] [21] [22]. The stated aim of grain growth enhancement is to improve fuel performance, such as reducing fission gas release (FGR) or minimizing pellet-cladding mechanical interaction. Previous research has highlighted oxides such as Cr_2O_3, CaO, MgO, Nb_2O_5, and TiO_2 among the dopants capable of enlarging grains; these oxides are subject to varying degrees of influence from the sintering atmosphere. Previous research generally indicates that sintering temperature, sintering atmosphere (oxidizing, inert, or reducing), holding time, and the type and concentration of dopants all significantly influence the final microstructure. Most contemporary fuel vendors are publicizing work on new fuel forms with performance benefits as the stated goal. For example, the addition of Cr_2O_3 (~700 ppm) and Al_2O_3 (~300 ppm) to UO_2 fuel has resulted in a significant increase in the resulting grain size from an average of 8 µm to 40 µm [23]. This work led to the classification of the modified fuel as a new product, called ADOPT® by Westinghouse.

This study explores the effect of Ni, Mo, and W dopants on the UO_2 fuel microstructure. These elements were chosen based on recommendations from previous studies and to provide a systematic evaluation of dopants representing different chemical configurations. The metals were incorporated into the fuel matrix in their primary oxide forms— NiO, MoO_3, and WO_3 —at concentrations ranging from 100 to 1000 weight parts per million (wppm) on a metals basis. The densification behavior and final microstructure were analyzed as a function of dopant concentration. Additionally, isotopic ratios of the feedstock were measured both before and after sintering to evaluate the retention of the chemical signature throughout the fabrication process.

2 Material and Methodology

2.1 *Powder production*

The UO_2 powder used in this study was derived from the reduction of natural-assay UO_3 powder supplied by Cameco Corporation, with a nominal purity of 99.9%. Given the focus on carefully evaluating dopant persistence throughout the processing, assessing the chemical impurities in the initial feedstock was a priority. The feedstock's chemical impurities were certified according to ASTM C753-16a [24] and further analyzed for additional impurities, with the results presented in **Table 1**.

Table 1: Composition of impurities in the UO_3 powder used as the initial feedstock material in this study.

Element	**Ag**	**Al**	**As**	**Ba**	**B**	**Ca + Mg**
Units in µg/g U	<0.12	<0.6	<0.15	<0.60	<0.13	<2.6
Element	**C**	**Cd**	**Cl**	**Co**	**Cr**	**Cu**
Units in µg/g U	19.5	<0.019	15.7	<0.30	1.4	<0.3
Element	**F**	**Fe**	**K**	**Mn**	**Mo**	**Na**
Units in µg/g U	<6	6	<0.50	<0.3	0.59	0.1
Element	**Nb**	**Ni**	**P**	**Pb**	**Ru**	**S**
Units in µg/g U	<0.1	<0.8	13	<0.25	<0.04	<4
Element	**Sb**	**Si**	**Sn**	**Sm/Gd/Eu/ Dy/Hf**	**Ta**	**Th**
Units in µg/g U	<0.25	2.0	<0.5	0.11	<0.05	<0.02
Element	**Ti**	**W**	**V**	**Zn**	**Zr**	
Units in µg/g U	<0.25	<0.13	<0.03	<0.5	<0.3	

The reduction of UO_3 to UO_2 was performed prior to mixing with the taggants. The reduction process began by heating the UO_3 powder in alumina crucibles to 573 K at a heating rate of 3°K/min, with a dwell time of 0.5 hours. The temperature was then increased to 1073 K at a rate of 5°K/min and held isothermally for 16 hours. Throughout the entire process, an atmosphere consisting of 4% H_2 and balance Ar (0.5 L/min) was maintained. After the reduction process, the resulting UO_2 powder was analyzed using X-ray powder diffraction (XRD) to confirm the crystallographic phases present. Additionally, weight measurements were taken before and after the process to assess the extent of reduction, revealing a total mass reduction of approximately 5.6%, which was consistent with the expected formation of UO_2.

The NiO, MoO_3, and WO_3 powders were synthesized by project collaborators at the Savannah River National Laboratory [25]. Two double-spike perturbed isotopic ratios were devised for each dopant element, defined in this study as A and B conditions. The isotopes altered for each ratio were chosen for either their low natural abundance (in the case of Ni and Mo) or relatively uniform abundance (in the case of W), facilitating easy identification of double-spike signature via mass spectrometry (MS) over the background natural isotopic content [7]. These dopant powders were

produced using a double-spike feedstock mechanism, which involved precise isotopic mixing in liquid form before drying to a powder condition. During isotopic mixing, the double-spike liquid feedstock was prepared using the ratios presented in **Table 2** before being added to a natural feedstock of the same element in a 1:5 ratio of spike-to-natural as reported in [26]. These "final" diluted forms are referred to as α and β [26]. As a final process step, the feedstock of the dopants was heated in a muffle furnace to produce the metal oxides.

Table 2: Nominal ratio of the isotopic double-spike dopant powder feedstocks used in this work. Note: These percentages are with respect to the enriched feedstocks used to make the taggant mixtures, not the specific isotopes. For example, Ni-A is not 50% ^{60}Ni; rather, 50% of Ni-A is the ^{60}Ni feedstock, which itself is 98.2 at% ^{60}Ni [26].

Dopant double-spike (ID)	Ratio of Feedstocks	
Ni-A	50% ^{60}Ni	50% ^{61}Ni
Ni-B	50% ^{60}Ni	50% ^{62}Ni
Mo-A	50% ^{94}Mo	50% ^{100}Mo
Mo-B	50% ^{92}Mo	50% ^{97}Mo
W-A	25% ^{184}W	75% ^{186}W
W-B	75% ^{184}W	25% ^{186}W

2.2 *Mixing batches and nomenclature*

The mixing batches of UO_2 powder and dopants were generated by milling in a high-energy mixer mill (Spex 8000M). The mixing proportions were adjusted to create two concentration levels—100 ppm (low) and 1000 ppm (high) — for each dopant species, with the values referring to the metal basis (i.e. Ni, Mo, and W to U by weight). For Ni, intermediate concentrations of 250 and 500 ppm were also prepared using natural isotopic NiO feedstock. The milling process was conducted for 30 min with batch sizes of approximately 15 g inside a new high-density polyethylene jar with 50 g of 3 mm yttria-stabilized zirconia milling spheres. To ensure accuracy when preparing the low-level (100 ppm) samples, the milled precursor powder at 1000 ppm was downblended with additional UO_2 to produce the desired concentration. The milled precursor powders then underwent a sieving process using a brass, 325-mesh sieve to ensure powder uniformity. Each type of dopant system (Ni-α, Ni-β, Mo-α, Mo-β, W-α, and W-β) had its own new milling spheres, sieve, lid, and sieve tray to prevent cross contamination of samples and irradiation campaigns. The list of produced mixtures and the nomenclature adopted throughout this study is presented in **Table 3**.

Table 3: Sample mixtures and their corresponding nomenclature used in this study.

Nomenclature	Sample	Nominal metal dopant concentration (ppm)	Isotopic double-spike
$\mathbf{Ni}_{\alpha}^{100}$	UO_2 doped with NiO	100	^{60}Ni, ^{61}Ni
$\mathbf{Ni}_{\alpha}^{1000}$		1000	
$\mathbf{Ni}_{\beta}^{100}$		100	^{60}Ni, ^{62}Ni
$\mathbf{Ni}_{\beta}^{1000}$		1000	
$\mathbf{Ni}^{250}$		250	Natural
$\mathbf{Ni}^{500}$		500	Natural
$\mathbf{Mo}_{\alpha}^{100}$	UO_2 doped with MoO_3	100	^{94}Mo,^{100}Mo
$\mathbf{Mo}_{\alpha}^{1000}$		1000	
$\mathbf{Mo}_{\beta}^{100}$		100	^{92}Mo, ^{97}Mo
$\mathbf{Mo}_{\beta}^{1000}$		1000	
$\mathbf{W}_{\alpha}^{100}$	UO_2 doped with WO_3	100	^{184}W, ^{186}W
$\mathbf{W}_{\alpha}^{1000}$		1000	
$\mathbf{W}_{\beta}^{100}$		100	
$\mathbf{W}_{\beta}^{1000}$		1000	

2.3 *Fuel pellet fabrication*

The powder blends were pressed in a uniaxial press using a stainless steel die and punch with a manual laboratory press (Carver Inc.). Prior to pressing, 0.25 wt% N,N'-ethylene bis-stearamide binder was added to the powders. A pressure of 200 MPa was applied for 2 minutes during the pressing process. Each pressed pellet was formed using approximately 0.4 g of the mixed batches, resulting in an average pellet diameter of 3.67 mm and thickness of 5.4 mm. The average green density of the pellets was measured at 6.88 g/cm³, which is approximately 62% of the theoretical density of pure UO_2 (10.97 g/cm^3) [27]. To minimize cross-contamination, a new die was used for each dopant system, and stearic acid was applied to the die and ram as a lubricant before pressing each pellet.

The pellets were sintered inside a refractory metal furnace (Materials Research Furnaces LLC) in an atmosphere comprising 4% H_2 and balance Ar (0.5 L/min) following the thermal profile outlined in **Figure 1**. For each sintering run, pellets of a specific dopant system were placed in W crucibles with a bed of fresh UO_2 powder. The same W crucibles were reused for all the sintering processes, and the powder bed was refreshed to avoid contamination between the samples and with the crucibles.

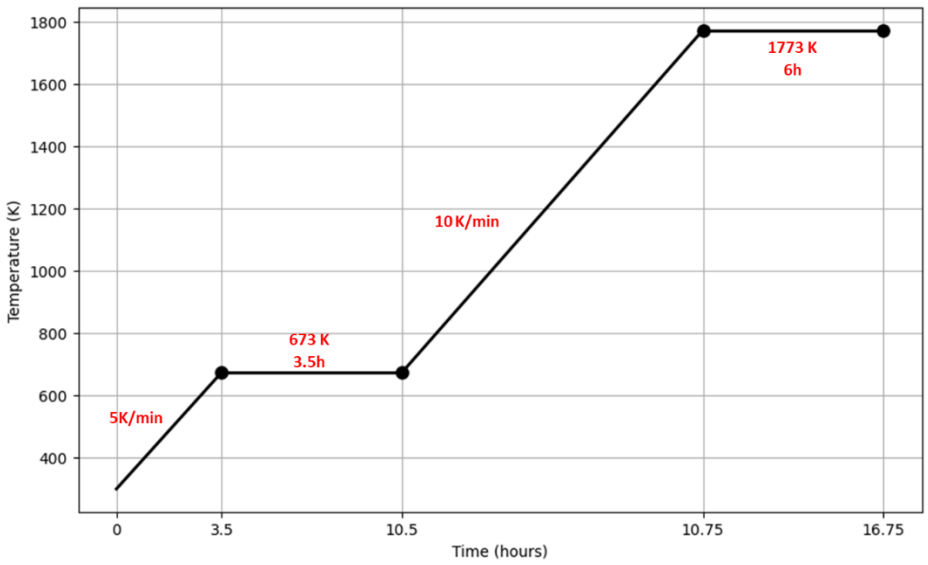

Figure 1: Thermal profile used for sintering the doped UO_2 pellets.

2.4 *Characterization*

2.4.1 Global chemistry: Elemental and isotopic ratios

The elemental and isotopic concentrations of dopants at various stages of fabrication (powder and sintered conditions) were analyzed using inductively coupled plasma optical emission spectrometry (ICP-OES) and inductively coupled plasma mass spectrometry (ICP-MS). All analyses were performed by the Chemical Isotopic and Mass Spectrometry Group at Oak Ridge National Laboratory.

The samples were transferred into perfluoroalkoxy vials and weighed along with their caps. Each vial was then supplemented with 8 mol/L HNO_3 for dissolution and heated on a hot plate at 383 K. Simultaneously, a Process Quality Control CUP-2 uranium ore concentrate certified reference material (CRM), along with two blanks, underwent digestion. Most of the sintered pellet samples were not fully digested under these conditions. To aid digestion, small quantities of concentrated HCl and HF were added to these samples, and the hot plate temperature was raised to 463 K. In case some solid persisted, samples underwent microwave digestion for 10 min at 473 K using a CEM Focused Microwave Discover SP-D Clinical System. In some cases, even after all digestion steps, some residual solid was still observed.

Fully digested samples had their solutions quantitatively transferred to a tared low-density polyethylene bottle and were stored in a mylar bag to prevent evaporation during subsequent analyses. This solution is referred to as the *master solution*. In the case of undissolved samples, the solids were segregated before being transferred into containers for the master solution. These undissolved samples often contained variously sized solid pieces, some settling easily while others remained suspended. To ensure complete collection of dissolved contents, samples underwent multiple rounds of centrifugation, decanting, and rinsing. This process ensured that all dissolved contents were effectively collected into the master solution container. The undissolved solids were slowly dried in a low-temperature oven and preserved for further analysis.

Before samples were sent for analysis, aliquots of the U matrix from the master solutions were separated from the trace elements using a solid-phase, extraction-based preparation technique. To achieve this step, samples were quantitatively loaded onto a diamyl amylphosphonate (UTEVA®) resin column. The U adhered to the resin, and the trace element fraction was collected separately. Following separation, the samples were dried on a hot plate and then reconstituted. From these dried, reconstituted samples, dilutions were made using high-purity 2% HNO_3, and the samples were subsequently submitted for trace metal and/or isotopic measurement [28].

Trace elemental analysis was conducted using an iCAP PRO (Thermo Scientific) ICP-OES detection platform with external calibration-based quantification. Measurement uncertainty was determined using an expanded uncertainty approach considering factors such as measurement uncertainty, calibration uncertainty, and quality control uncertainty (percent relative difference). For this analysis, laboratory control samples included two CRMs certified for trace elements in a U (U_3O_8) matrix: one from the New Brunswick Laboratory Program Office (CRM 124-1) and one U ore concentrate sample (CUP-2). Measurements of CRM 124-1 and CUP-2 were conducted throughout the entirety of the sequences. The results showed excellent agreement between the measured values and the certified or consensus values.

Isotopic measurements were conducted using a Thermo Fisher Scientific Neoma Multi-collector ICP-MS. Prior to each analysis, a blank consisting of high-purity 2% HNO_3 was measured in the same manner as the unknowns and standards. To correct for mass bias, monitor instrument stability, and address instrumental drift, standards were interspersed at regular intervals among all the unknowns. Because of a lack of CRMs for the elements of interest, single-element solutions manufactured by High Purity Standards were used as mass bias and control standards. Mass bias corrections were applied using each element's isotopic composition as adopted by the International Union of Pure and Applied Chemistry. An automated peak centering routine was applied to each standard analysis. Prior to the start of each sequence, an instrumental Faraday cup gain and baseline correction regime were executed for the three different elemental systems. Raw voltage data observed during each acquisition cycle were exported from the instrument and subsequently processed offline, including steps such as blank subtraction, mass bias correction, and uncertainty calculation.

2.4.2 Pellet density and microstructure

Pellet densities were determined by measuring sintered pellet dimensions in triplicate using a micrometer (Mitutoyo 500-195-30). The median value from these measurements was used to calculate the density in grams per cubic centimeter. The percentage of theoretical density was calculated based on fully dense UO_2, which has a density of 10.97 g cc^{-1} (10.97 kg m^{-3}).

For each dopant system, one pellet underwent cross-sectioning, polishing, and analyzing in optical (OM) and scanning electron microscope (SEM) to capture representative images of the pellet microstructure as fabricated. Transverse sections of the pellets were prepared using a diamond blade sectioning saw. Following sectioning, the pellets were polished using a Struers TegraPol-15 polisher equipped with Struers polishing pads and diamond suspensions of 6, 3, and 1 µm. The final polishing step involved using a 0.02 µm colloidal silica suspensions to achieve the desired surface finish for SEM analysis.

Optical microscopy was conducted using Leica DMRX microscope equipped with ImagePro Plus software. A Phenom XL desktop tabletop SEM was used to image the pellet center and regions

near two opposite edges. Grain size was determined from SEM images by manually measuring grain boundaries within rectangular image regions measuring 70.5 × 71 mm, which is equivalent to a 5000 mm² rectangle, following the planimetric procedure outlined in ASTM Standard E112-12 [29]. Image magnifications for grain size analysis were selected to ensure that a minimum of 50 grains were present within the rectangle while also maintaining a practical maximum number of grains to ensure that grains remained easily distinguishable.

2.4.3 Crystallographic lattice and local chemistry

Lattice parameter changes in the tagged UO_2 samples were investigated using X-ray diffraction (XRD). Samples weighing 100–200 mg were finely ground with a mortar and pestle, then deposited onto a zero-background silicon (Si) substrate for analysis. XRD measurements were conducted using a Proto AXRD benchtop diffractometer configured in Bragg–Brentano geometry, equipped with a Cu Kα radiation source (λ = 1.5406 Å) and a Dectris Mythen 1D detector.

To minimize beam divergence, a 1 mm incident divergence slit and diffracted-beam Soller slits were used. Data were collected over the range of $20° \leq 2\theta \leq 120°$, with a dwell time of 3 seconds per step and a step size of 0.02°. The 2θ offset was corrected by referencing the known peak positions of a LaB_6 standard that was added to the sample for this analysis. Experimental data were refined using the MAUD software package [30] . The UO_2 lattice parameter for each sample was determined by correcting for sample displacement while maintaining the LaB_6 structure constant during the refinement process [31].

The effect of dopant incorporation on the local structure of UO_2 was investigated using Raman spectroscopy [32]. Raman spectroscopic data were acquired using a Renishaw inVia Qontor micro-Raman spectrometer with a 633 nm excitation laser and a 50× objective. An automated, high-speed, optically encoded sample stage facilitated *XY* mapping with a step size of 1 µm and five spectral accumulations for each step. Data processing was carried out using WiRE 5.5 and Origin Scientific software. Peak positions were determined from the full width at half-maximum values identified through fitting procedures.

3 Results

3.1 Elemental and double-spike retention through fabricant process

The retention of elemental dopants throughout the fabrication process was evaluated by performing elemental analysis on both the mixed powder batches and the corresponding sintered pellets using ICP-OES. Results for each dopant system—including the mean value, lower and upper whiskers (representing values below the 15th percentile and above the 75th percentile, respectively), and analytical error—are presented in **Figure 2**.

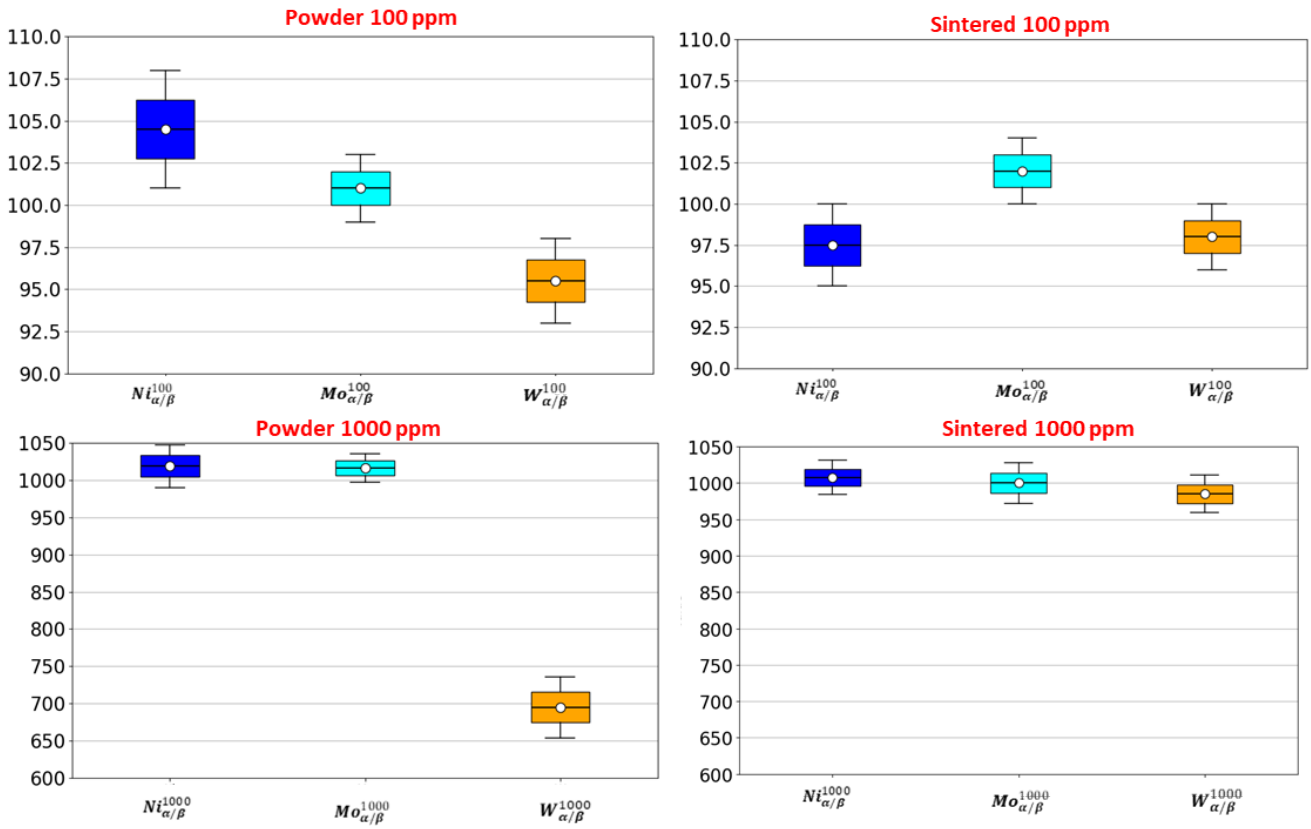

Figure 2: Whisker plots of elemental dopant concentrations in both powder and sintered pellets, as measured by ICP-OES. Each plot shows the average value (central dot) and the associated standard error of the measurement.

For the Ni and Mo dopant systems, the intended concentrations were maintained through to the final sintered fuel pellets across all compositions. However, a deviation between the powder and sintered values was observed for the W system at the 1000 ppm composition, where a notably lower concentration was detected in the mixed powder. Since the sintered value for $W_{\alpha/\beta}^{1000}$ closely matched the target composition—and given that the sintered pellet originated from the same powder batch—this discrepancy may be attributed to a measurement error, possibly resulting from incomplete dissolution during the ICP-OES sample preparation process.

To evaluate the preservation of the double-spike isotopic signature, isotopic concentration analysis was conducted on powder samples for the Mo and W systems, and on pellet samples for the Ni system, all at the highest concentration level (1000 ppm). The results are presented in

Figure 3. As shown, the double-spike isotopic barcodes were detectable across all systems. In the Ni system, the inversion in concentrations of ^{61}Ni and ^{62}Ni enabled clear differentiation between the *α* and *β* samples. Similarly, in the Mo system, higher concentrations of ^{94}Mo and ^{100}Mo identified the *α* samples, while ^{92}Mo and ^{97}Mo were more prevalent in the *β* samples. Distinctive markers of ^{184}W and ^{186}W were also measurable in the W-doped samples.

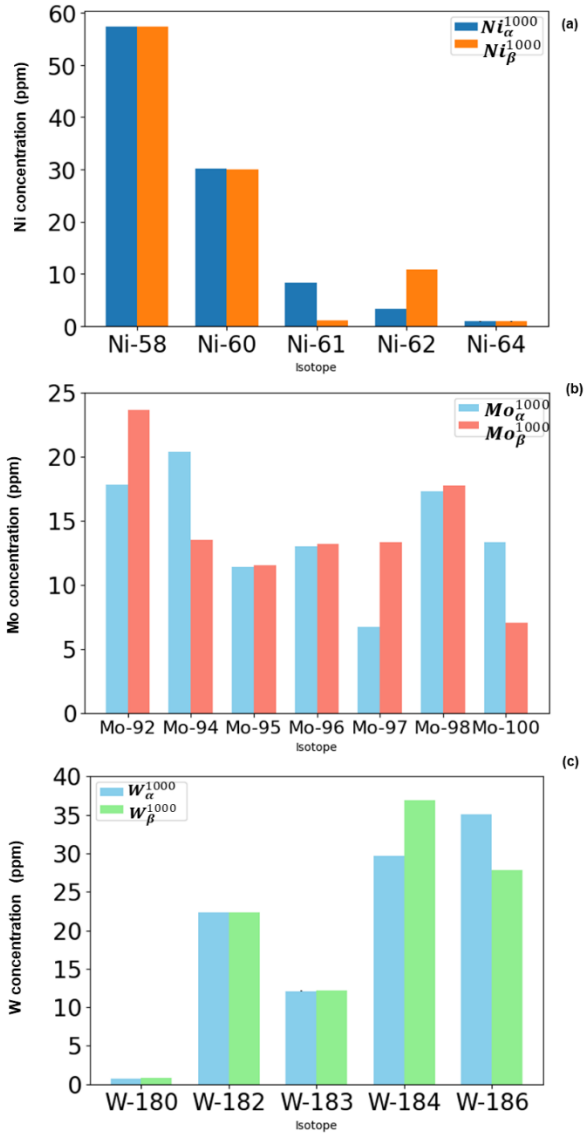

Figure 3: ICP-MS isotopic ratios for 1000 ppm doped UO_2 samples. Measurements were conducted on (a) Ni-α/β in sintered pellets, and (b) Mo-α/β and (c) W-α/β in the mixed powder state.

3.2 Doped fuel pellet microstructure

To partially evaluate the effect of dopant incorporation on fuel performance, several key fuel specification parameters were analyzed. One critical parameter examined was the final sintered

density, which plays a significant role in FGR and fuel swelling. The theoretical density values of each sintered pellet, along with the corresponding average density for each dopant system, are presented in **Figure 4.**

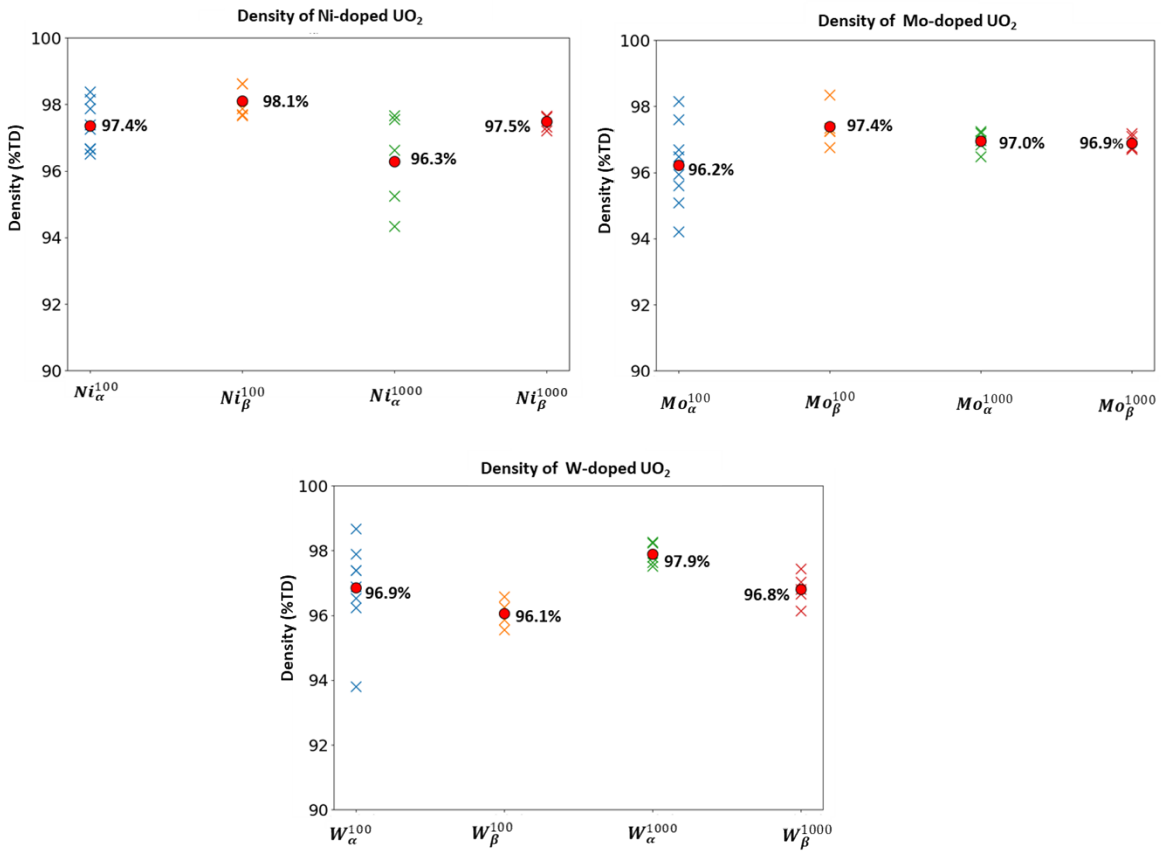

Figure 4: Sintered theoretical density of individual of individual UO_2 pellets (x) doped with Ni, Mo, and W at 100 and 1000 ppm, along with average density for each dopant system (red dot).

Across all dopant systems, increasing the concentration from 100 to 1000 ppm did not produce a significant change in the final sintered density. The highest average theoretical density was observed in the 100 ppm Ni-*β* system, reaching up to 98.1%, while the lowest was recorded for the 100 ppm W-*β* system. Overall, the sintered densities obtained in this study fall within the typical commercial specifications for UO_2 fuel, which generally range from 94% to 97%, depending on the reactor design (e.g., pressurized water reactor or boiling water reactor) [33] [34].

Another parameter commonly included in fuel pellet specifications is the average grain size. Representative microstructures for each dopant system, at both concentration levels and from distinct pellet regions, are shown in **Figure 5** through **Figure 7**. The corresponding average grain sizes measured in each pellet area are plotted in **Figure 8**. For reference, grain size data for undoped UO_2 pellets—fabricated using the same feedstock and sintered under identical

conditions—are also included to highlight the effect of taggant incorporation on grain growth behavior.

The Ni dopant produced the largest average grain sizes among the systems studied. A clear compositional effect was observed, with lower concentrations (100 ppm) promoting greater average grain growth compared to higher concentrations (1000 ppm). At 100 ppm, Ni appeared to moderately enhance grain growth relative to undoped UO_2. However, increasing the Ni concentration led to a noticeable reduction in grain size, decreasing from approximately 9 μm to around 5.5 μm.

For the Mo and W systems, the average grain size was noticeably reduced at both concentration levels compared to the pure UO_2 reference material, indicating a clear influence of these dopants on the fuel microstructure. A degree of heterogeneity in grain distribution was observed for these elements, with a mixture of fine and larger grains, particularly toward the edge of the pellet. However, variations in dopant concentration did not result in statistically significant differences in grain size for either system. Interestingly, a slightly smaller grain size was observed at the center of the pellets, which contrasts with the trend seen in both the pure UO_2 and Ni-doped systems, where grain growth was typically more pronounced at the center. Evidence of precipitate formation was observed in all high-concentration samples, with supporting optical micrographs provided in **Appendix A**.

An overall comparison of the total average grain sizes for all systems is presented in **Figure 9**, including valuer for the Ni middle composition 500 ppm and the acceptable range for commercial UO_2 fuel, which typically spans from greater than 6 μm to less than 25 μm [35]. The grain size observed for the Ni^{100} sample fell within this commercially acceptable range, indicating its potential compatibility with current fuel performance standards.

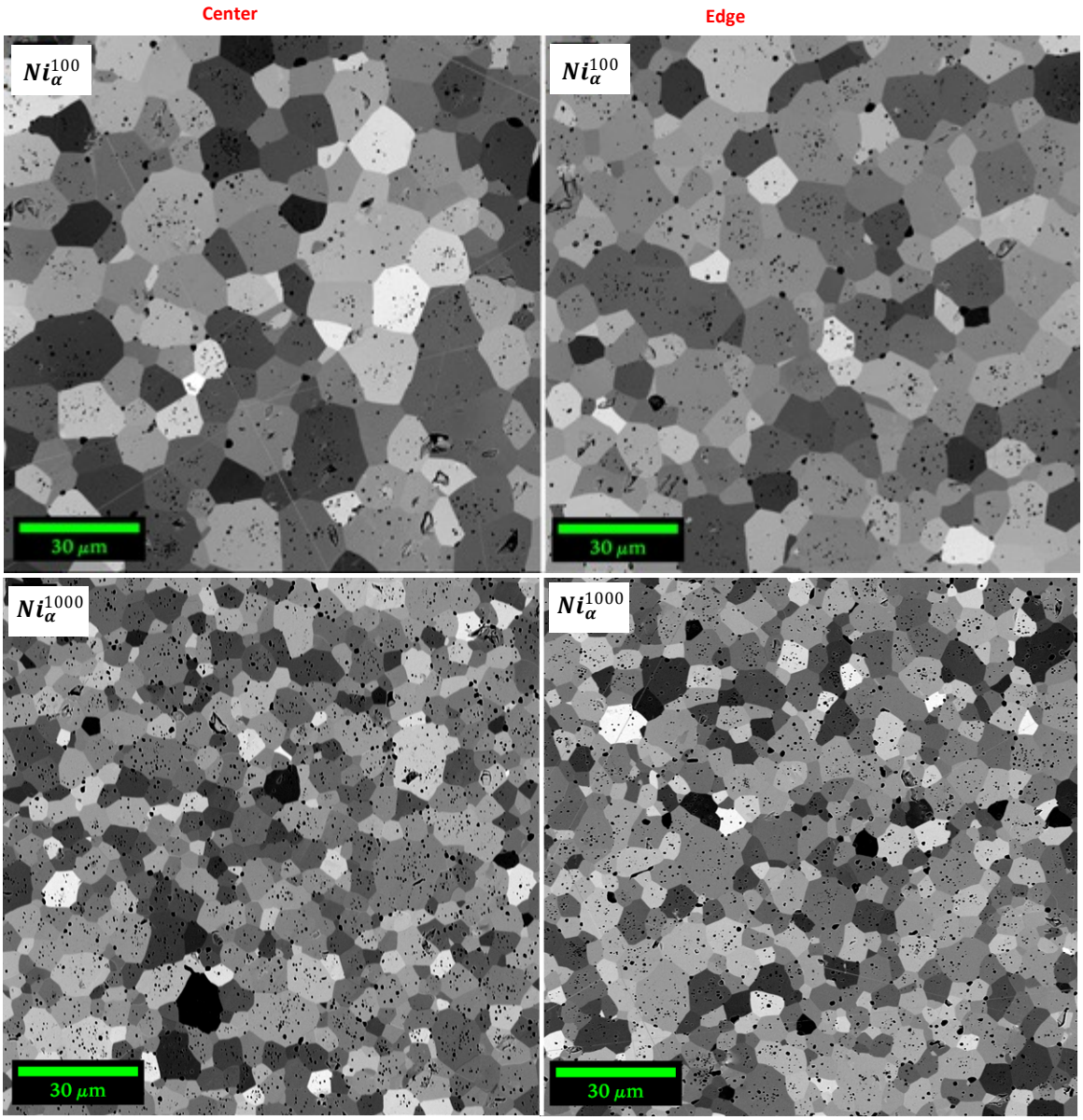

Figure 5: SEM micrographs of Ni-doped UO_2 samples showing (top) Ni_{α}^{100} and (bottom) Ni_{α}^{1000} near pellet center and near pellet edge.

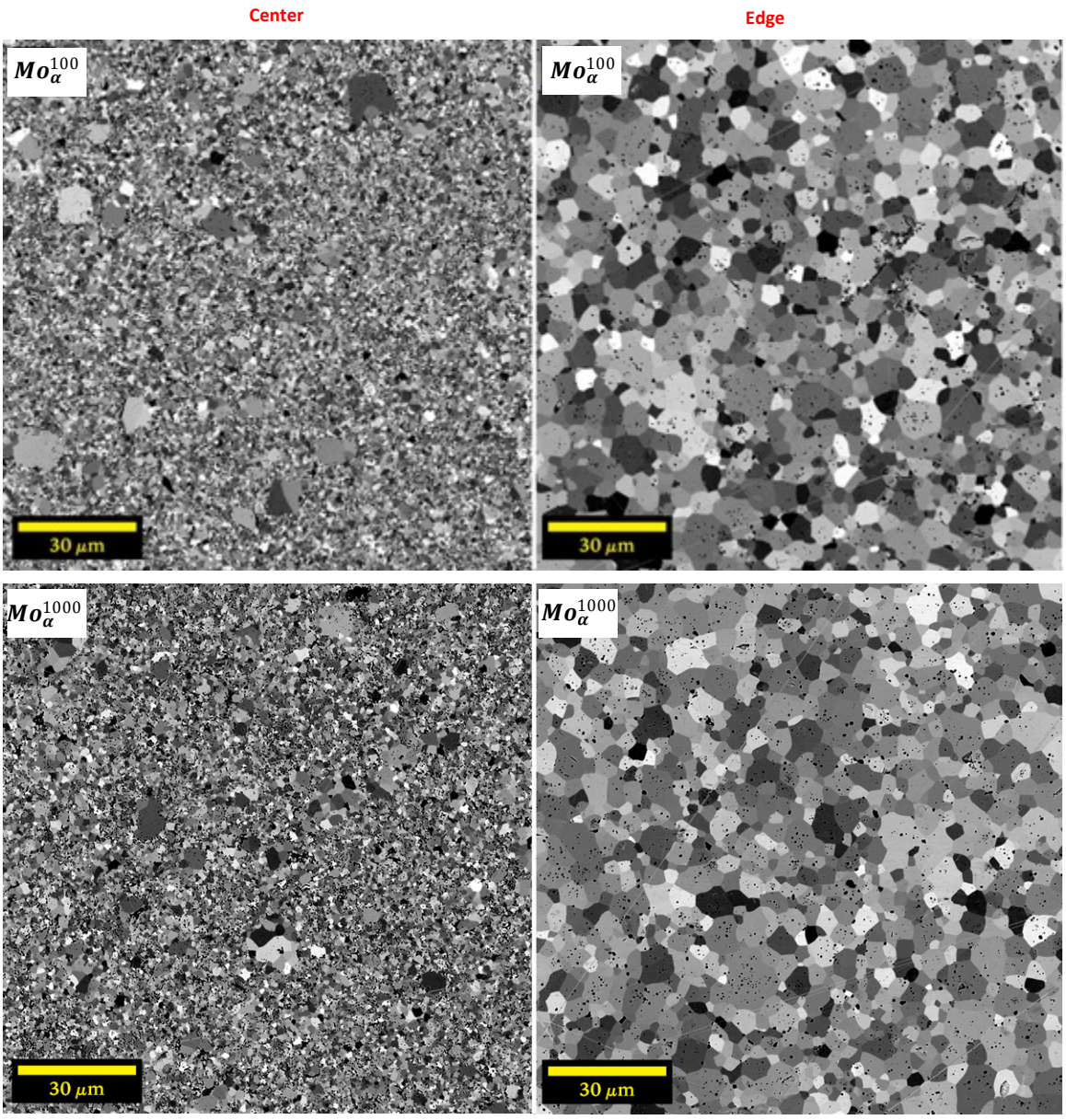

Figure 6: SEM micrographs of Mo-doped UO_2 samples showing (top) Mo_{α}^{100} and (bottom) Mo_{α}^{1000} near pellet center and near pellet edge.

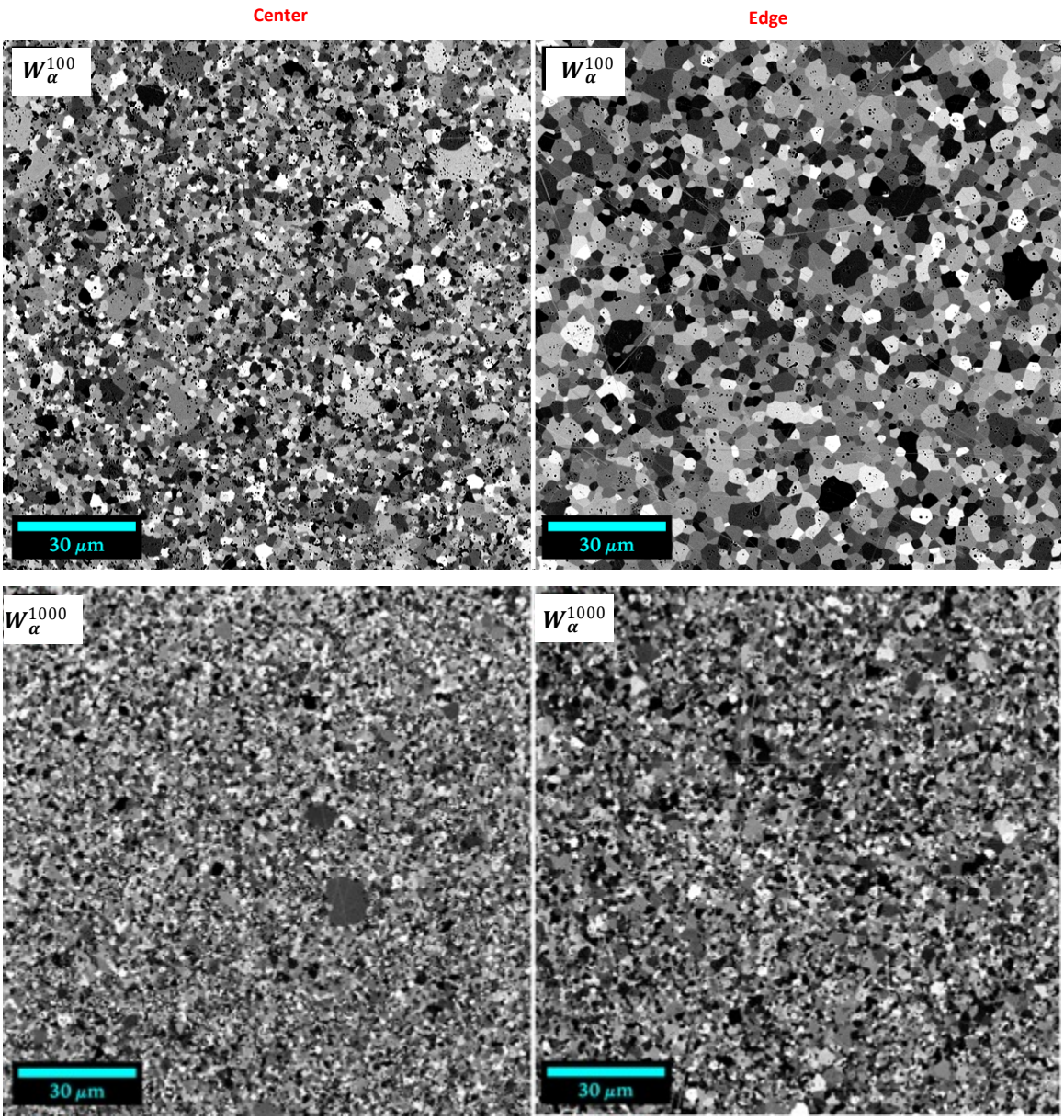

Figure 7: SEM micrographs of W-doped UO_2 (top) W_α^{100} and (bottom) W_α^{1000} near pellet center and near pellet edge.

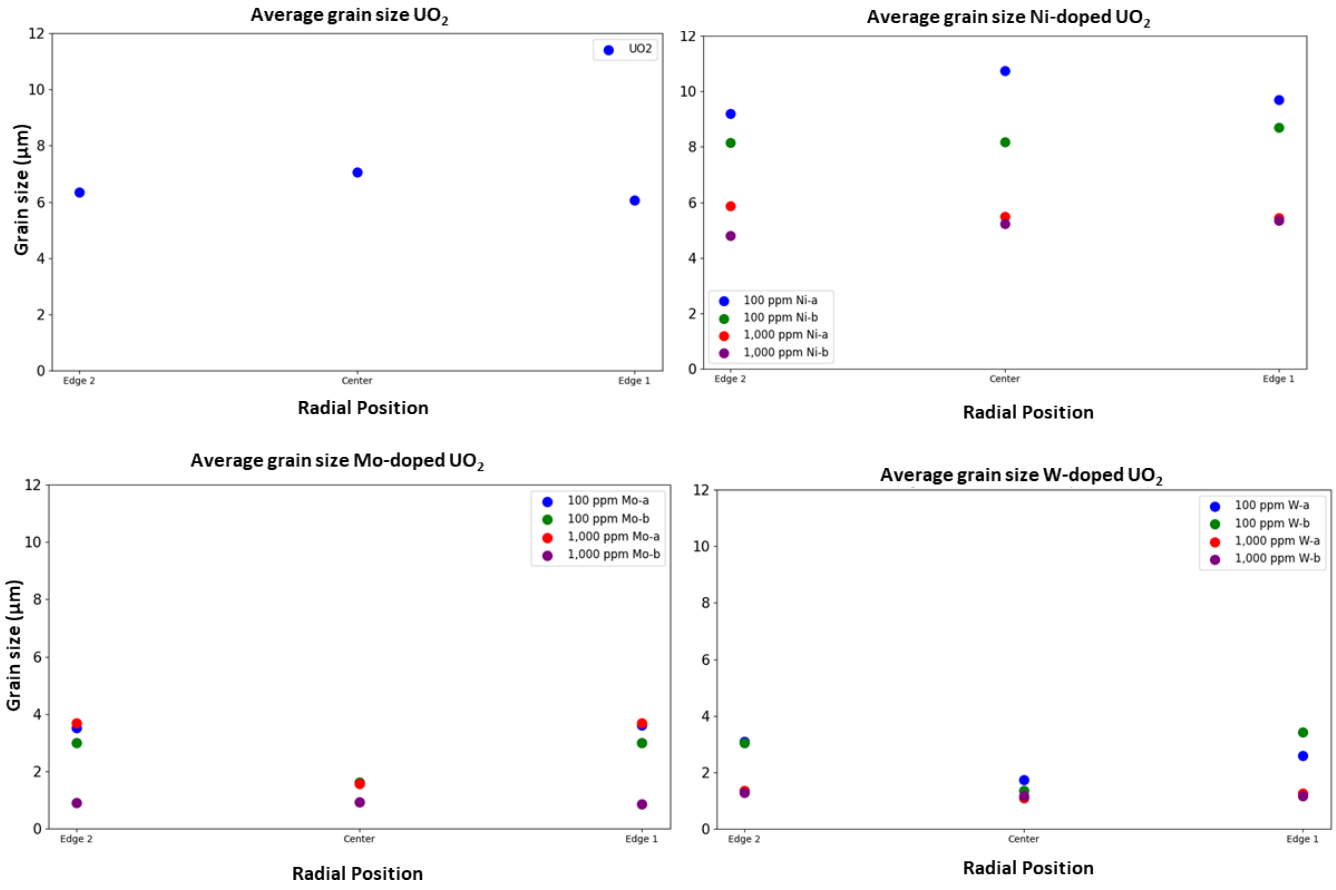

390

391 **Figure 8:** Average grain size measured at three distinct locations within the sintered pellet for UO_2 samples
392 doped with Ni, Mo, and W**.**

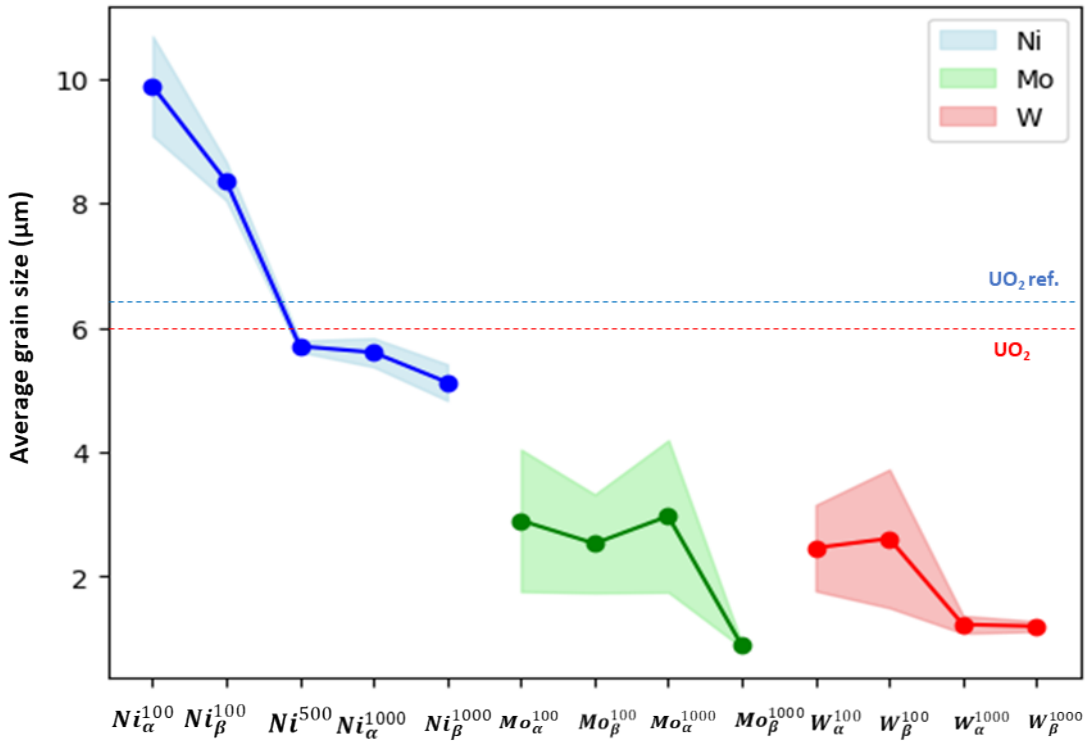

Figure 9: Average grain size and associated standard deviation for Ni-*α/β*, Mo-*α/β*, and W-*α/β* doped UO_2 at 100 and 1000 ppm concentrations, including an additional data point for Ni^{500}. The horizontal reference line indicates the minimum acceptable grain size specified for commercial UO_2 fuel (red) and the UO_2 reference sample (blue).

3.3 Crystallographic lattice distortion and local chemistry

To further assess the effect of dopants on the behavior of the fuel matrix, their influence on the crystal lattice was evaluated using XRD. Representative diffraction patterns for the *α*-series doped samples are shown in **Figure 10**, with a reduced 2*θ* range selected to improve visualization. The diffraction analysis identified only two crystalline phases: UO_2 and LaB_6. As expected, no separate phases corresponding to NiO, MoO_3, or WO_3 were detected, likely due to the low dopant concentrations. Additionally, the lattice parameters of the UO_2 phase, obtained through Rietveld refinement, are presented in

Figure 11.

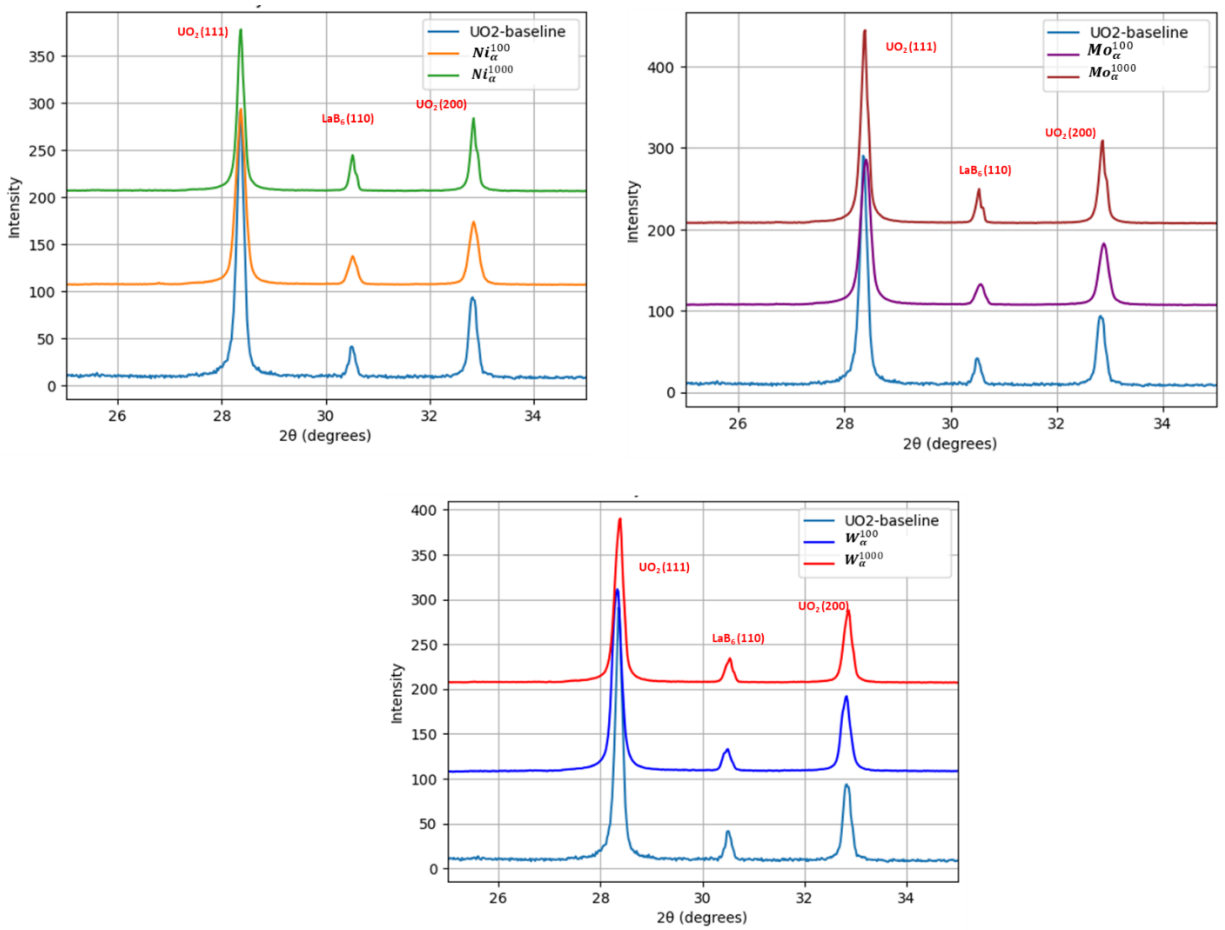

410

411 **Figure 10:** XRD patterns of UO_2 pellets doped with Ni, Mo, and W from the α series. Patterns are shown
412 over a reduced 2θ range (25° to 35°) to enhance visualization of key diffraction peaks.

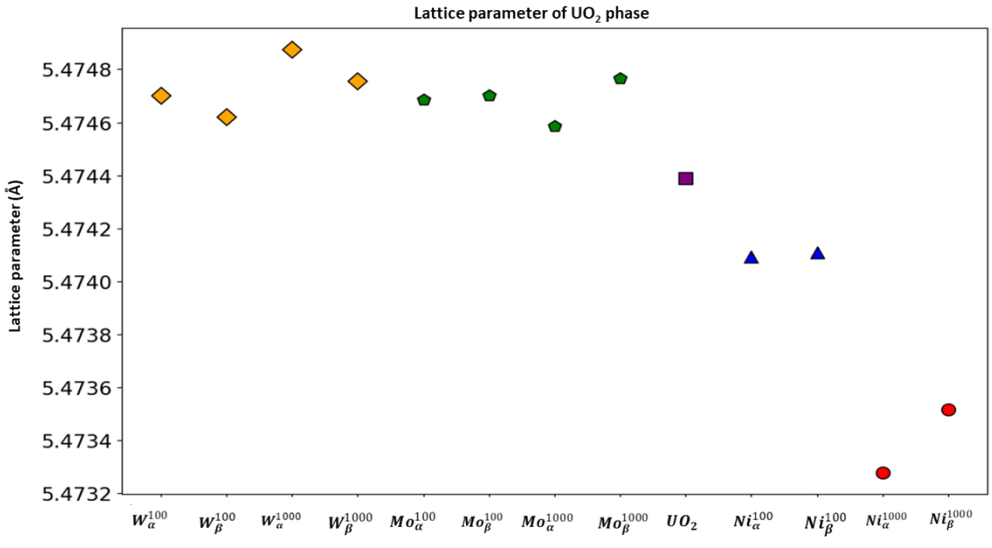

413

414 **Figure 11:** UO_2 lattice parameter obtained for pure UO_2 (used as precursor material) and UO_2-doped
415 pellets with Ni, Mo, and W.

To evaluate the maximum solubility of Ni in the UO_2 lattice, additional samples containing NiO at concentrations of 250 and 500 ppm were included in the study. The resulting lattice parameters as a function of Ni concentration are shown in **Figure 12**. A progressive lattice contraction was observed with increasing Ni content up to 500 ppm, beyond which the lattice parameter closely matched that of the 1000 ppm sample. These results suggest that the solubility limit of Ni in UO_2, under the fabrication conditions used in this work, is approximately 500 ppm.

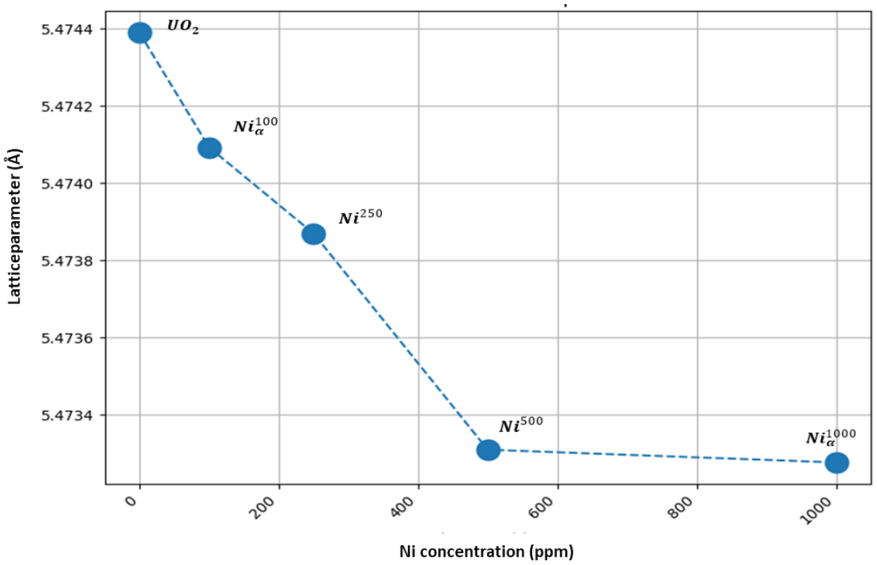

Figure 12: UO_2 lattice parameter as a function of Ni concentration for 0, 100, 250, 500, and 1000 ppm.

To investigate potential local structural distortions resulting from dopant incorporation in UO_2, Raman spectroscopic analysis was performed (**Figure 13**). The most prominent feature observed in the Ni–UO_2 samples was the T_{2g} vibrational mode near 445 cm^{-1}, which is characteristic of the fluorite structure and corresponds to the symmetric vibration of oxygen atoms around uranium atoms. The presence of this peak indicates that the structural integrity of the UO_2 lattice is largely preserved during Ni incorporation.

Additionally, the longitudinal optical (LO) phonon mode at approximately 575 cm^{-1} and its overtone (2LO) near 1150 cm^{-1} were also observed. Both peaks exhibited reduced intensity with increasing Ni content, suggesting increased lattice disorder and providing further evidence for Ni incorporation into the UO_2 lattice. This behavior is consistent with Ni^{2+} substituting for U^{4+}, with accompanying oxygen vacancies introduced to maintain charge neutrality [36] [37] [38].

Importantly, no evidence of tetragonal sublattice ordering was found, which would typically appear as a defect band near 630 cm^{-1}. A broad, low-intensity mode was observed near 910 cm^{-1}, but this feature does not correspond to any known defect structures in UO_2.

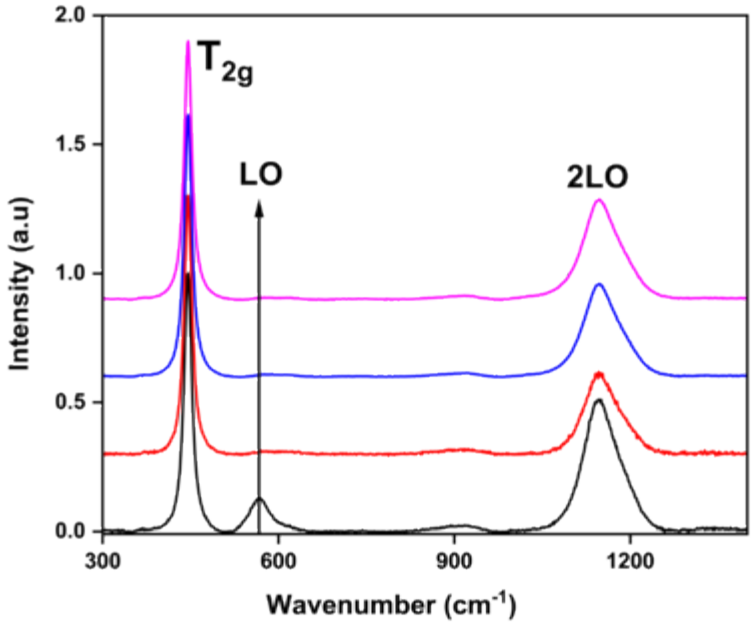

Figure 13: Averaged Raman spectra for undoped UO_2 (black), $\boldsymbol{Ni}^{250}$ (red), $\boldsymbol{Ni}^{500}$ (blue), and $\boldsymbol{Ni}_{\boldsymbol{\alpha}}^{1000}$ (magenta). Baselines have been vertically offset for clarity.

4 Discussion

4.1 Tagged fuel chemistry

The potential volatility of additives in UO_2 under sintering conditions is a well-recognized challenge within the nuclear fuel community. For example, although Cr has been extensively studied as a dopant [39] , experimental investigations have consistently shown that sintering UO_2 with Cr_2O_3 under reducing conditions often results in nearly complete loss of Cr due to its volatility [22]. [22]. Similarly, Mn has been identified through modeling as a strong promoter of grain growth [40] , but efforts to sinter $UO_2$with MnO have encountered significant Mn loss, complicating both synthesis and evaluation of its potential performance benefits [41] . Given these challenges, verifying the final composition of UO_2 materials with targeted chemical modifications is crucial—particularly when dopants are intended for nuclear forensics applications..

The chemical analysis performed in the present work revealed that the initial dopant values introduced into the powder were fully retained throughout the fabrication process up to the final sintered fuel pellet (**Figure 2**). This result indicates that the incorporation of Ni, Mo, or W dopants into UO_2 pellets can be effectively achieved with neither significant loss or alteration of the dopant composition nor significant change in the current fabrication process.

The isotopic chemical analysis further confirmed the detectability of the double-spike signature in all dopant systems (**Figure 3**), demonstrating the robustness of the tagging mechanism—even when blended with natural feedstock. As shown in the figure, clear differentiation between dopant α and β variants was achieved across all systems. For the Ni-*α* and Ni-β samples, the distinct ^{61}Ni

and ^{62}Ni isotopic spikes were detected and persisted through the final sintering process under a reducing atmosphere. Similarly, in the Mo system, the characteristic double-spike signatures—^{94}Mo and ^{100}Mo for Mo-*α*, and ^{92}Mo and ^{97}Mo for Mo-*β*—remained clearly discernible in the final mixed powder condition. In the W-doped system, inversion in the concentrations of ^{184}W and ^{186}W between W-α and W-β samples was also evident demonstrating viability of use of this double-spike signature in this system. These findings provide strong confidence that the isotopic taggant barcodes were preserved and remained detectable throughout the fuel fabrication process. However, further studies are required to determine the optimum dilution level, i.t at which an isotopic double-spike remains reliably detectable but minimum disturbance in fuel performance is achieve, under the current material processing conditions.

4.2 Tagged fuel microstructures and crystallography

Dopant incorporation into fuel pellets produced varying impacts on the resulting pellet microstructure. While no significant effect on the final sintered density was observed across different compositions or dopant systems (**Figure 4**), the grain size exhibited clear and distinct responses depending on the type and concentration of dopant.The Ni-doped system exhibited an inverse relationship between grain size and dopant concentration (**Figure 8** and **Figure 9**). Lower Ni concentrations were associated with larger grain sizes compared to pure UO_2. These samples also showed a measurable contraction in the UO_2 lattice parameter (

Figure 11), indicating successful Ni incorporation into the lattice. Further investigation into the solubility limit revealed that up to 500 ppm of Ni can be retained in solid solution under the studied conditions. Samples with lower Ni concentrations (within the solubility limit) produced grain sizes that fall within the acceptable range for commercial fuel specifications. In contrast, higher Ni concentrations (1000 ppm) resulted in reduced grain sizes relative to the lower concentration samples.

In the Mo and W systems, a significant reduction in grain size was observed across all compositions studied. This grain size reduction was statistically insensitive to changes in dopant concentration, suggesting minimal or no solubility of Mo or W in the UO_2 lattice under the current fabrication conditions. The reduced grain sizes in these systems are likely caused by limited grain boundary mobility, potentially due to the formation of secondary phases within the oxide matrix that inhibit grain growth (see **Appendix A**).

As anticipated, all the dopant systems displayed minor alterations in the diffraction pattern compared with pure UO_2. The overall observed behavior can be categorized in two ways. First, with the Mo and W dopants, no correlation of the lattice parameter was detected as a function of composition, and all the samples for these systems presented a slight expansion of lattice parameters when compared with pristine UO_2 (

Figure 11). This result may be correlated with the types of defects present in UO_2, such as oxygen vacancies, which introduce structural distortions into the lattice. A similar trend was reported by Vazhappilly et al. [42], using first-principles calculations to demonstrate that the incorporation of Ln^{3+} atoms into the UO_2 lattice leads to an increase in the lattice parameter even when the replace atom is smaller. This effect was attributed to a reduction in the attractive electrostatic interaction between the cations and surrounding lattice. In addition, the formation of oxygen vacancies,

required to maintain charge neutrality with Ln^{3+} substitution for U^{4+}, was found to increase electrostatic repulsion, further contributing to the overall lattice expansion.

Second, for the Ni dopant, the lattice parameters suggested a structural dependence on the composition, resulting in an overall contraction in the lattice parameter with increasing Ni concentration. This trend suggested the possible incorporation of Ni into the UO_2 matrix, likely occurring via incorporation on U cation sites.

The thermodynamic behavior of the Ni–U–O and W–U–O systems has not been extensively evaluated in the open literature. The effect of Ni on UO_2 microstructure was previously investigated by Zhong et al. [18] , who reported a reduction in grain size with Ni addition—an observation consistent with the present findings. However, the Ni concentrations examined in that study were significantly higher (~ 5000 ppm) than those explored here, limiting the potential for direct comparison. In contrast, the current work demonstrates—for the first time—the solubility of Ni in UO_2 to be constrained to approximately 500 ppm, providing new insights into dopant behavior at more practical and industrially relevant concentrations.

The thermochemistry of Mo in UO_2 has received more attention than other dopants due to its presence as a fission product. The chemical state of Mo—specifically whether it exists as a metallic precipitate, MoO_2 precipitate, or is dissolved as Mo^{4+} on uranium lattice sites—has been the subject of ongoing debate over the past few decades [43]. While several studies have investigated the chemical form of Mo in irradiated UO_2, fewer have focused on the intentional synthesis of UO_2 with Mo or Mo oxides, as carried out in the present work.

Kleykamp conducted foundational studies synthesizing UO_2 with Mo and MoO_2 additions as part of a evaluation strategy to study fission product thermochemistry [44]. That work reported very low solubility limits for Mo and MoO_2 in UO_2—approximately 20 ppm and 60 ppm, respectively. Another study used a processing methodology similar to that of the present investigation but evaluated much higher Mo concentrations (1%–15%). That study observed lattice expansion effects consistent with Mo incorporation [45] and concluded that up to 4 atom % Mo can be retained in solid solution.

In contrast, the current study focuses on the dilute doping regime, specifically evaluating the influence of low Mo concentrations on the microstructure of UO_2. A significant grain size reduction was observed across all Mo-doped compositions, which is consistent with limited solubility—in agreement with the findings reported by Kleykamp. These results indicate that even small additions of Mo can strongly affect grain growth behavior. However, further investigation is needed to accurately quantify the solubility limits of Mo under the specific processing conditions employed in this work.

4.3 Hypothesized impact of taggants on fuel performance

Light-water reactor (LWR) fuel rods are engineered to accommodate the expected release of fission gases over their operational lifetimes. However, modifications to fuel compositions that increase total gas release, combined with industry efforts to extend reactor lifespans and achieve higher burnup levels, raise concerns about the ability of current fuel designs to manage the resulting elevated internal pressures. This issue is particularly critical, as the generation, transport,

and release of gaseous fission products can significantly influence the thermomechanical behavior of the fuel and the integrity of the fuel–cladding system, ultimately impacting overall reactor safety and performance.

The effect of a candidate taggant on fuel performance is one key factor in the viability of intentional forensics as a method to improve the speed and reliability of material provenance assessments. Historically, fuel vendors in the US had to undergo a rigorous qualification process with the US Nuclear Regulatory Commission to demonstrate the performance and safety aspects of any new reactor materials. This process involved lead test rods (LTRs) and lead test assemblies (LTAs), followed by post irradiation examination, to compile a topical report for submission to the regulatory agency [13]. This process was not only costly but also time-intensive, requiring sequential irradiation and post irradiation examination tests. For example, the introduction of Cr-doped pellets in the US took approximately 10 years to obtain licensing [46].

The dopants and concentrations evaluated in this study exhibited varying effects on the microstructure of UO_2. While all doped samples maintained comparable final sintered densities, significant differences in grain size were observed—ranging from approximately 5 to 10 μm for Ni-doped samples, and 1 to 3 μm for Mo- and W-doped samples. These variations in grain size could influence fuel performance under irradiation. Turnbull's work demonstrated that smaller grain sizes enhance grain boundary connectivity, thereby accelerating gas transport and increasing FGR in UO_2 [47] . In comparative irradiations of UO_2 samples with average grain sizes of 7 μm and 40 μm, exposed to 1750°C and up to 4% FIMA, FGR decreased by more than a factor of 2.3 in the larger-grained material. Additionally**,** fuel swelling was significantly reduced in the large-grained sample, with Turnbull reporting a 1.7× increase in swelling for the smaller-grained 7 μm UO_2 [47] . This behavior is consistent with the conventional understanding that swelling is inversely correlated with grain size, as finer grains increase the volume fraction of interconnected grain-edge tunnels that accommodate and transport fission gases [48] .

More recent irradiations of doped UO_2 have confirmed the general trend reported by Turnbull but have also highlighted that factors other than grain size play a major role in fuel performance. The ability of Ni to reside on U sites of UO_2 up to concentrations of approximately 500 ppm was confirmed in the present work, and effects of Ni on the local defect chemistry were confirmed by Raman spectroscopy. The ability of dopants to perturb the structure of UO_2 and, in doing so, affect diffusion phenomena and the resulting fuel performance has been investigated using atomistic modeling. Recently, work by Cooper et al. [40] [49] investigated the effects of Mg, Ti, V, Cr, Mn, and Fe on the thermal diffusion in UO_2 via first-principles methods, proposing an explanation for the enhanced diffusion caused by these dopants. Their work proposed that the inclusion of such elements can create charged interstitials, which enhance the population of U vacancies in the system at high temperatures. The increased concentration of U vacancies leads to enhanced atomic self-diffusion, which is the principal driver of diffusion in the fuel matrix, including the diffusion of fission products. Therefore, even in small quantities, dopants can promote a significant shift in UO_2 performance with respect to fission gas diffusion and the resulting bubble morphology, microstructural evolutions induced by temperature, in-pile densification, and other behaviors.

Considering only the basic correlations between grain size and FGR, the highest FGR is expected to be observed for UO_2 tagged with 1000 ppm Mo or W because of their smaller grain sizes. The

UO_2 tagged with Ni at the concentrations studied here would be expected to parallel the behavior of UO_2 given the minimal effect on microstructure. Within its solubility range, Ni doping was observed to promote moderate grain growth, providing evidence of its role in enhancing self-diffusion within the UO_2 matrix. This suggests that the solubility of Ni in UO_2 may overcome the grain size effect alone for FGR. Such influences may become particularly pronounced under high-temperature irradiation conditions, where diffusion-driven mechanisms dominate microstructural evolution and gas transport behavior.Historic investigations of the role of dopants on FGR in UO_2 have reported that Ti and Nb present in UO_2 can increase the effective diffusion coefficient for the mobility of Kr atoms by up to five orders of magnitude, greatly surpassing the effect of grain size alone [50]. The effect of the increased diffusion of gas atoms induced by the lattice defects of doped UO_2 would persist even if the as-fabricated grain size is affected by restructuring during service, which is anticipated in the central regions and outer rim of light-water reactor fuels [51].

The doped UO_2 samples characterized in this work are currently undergoing irradiation using the MiniFuel vehicle at Oak Ridge National Laboratory's High Flux Isotope Reactor (HFIR), to study the radiological effects on the taggants [21]. The irradiation conditions were structured with a total of three targets, each containing six MiniFuel capsules, resulting in the irradiation of 18 tagged specimens in total. These specimens were sealed in Mo capsules and subjected to irradiation for varying periods corresponding to three, five, and six cycles at HFIR (where each cycle lasts approximately 25 days), maintaining an irradiation temperature of approximately 600°C throughout the process [52]. This temperature is not anticipated to induce restructuring, and therefore, FGR and swelling measurements following irradiation will provide a key indication on the viability of the taggants for expanded study.

5 Conclusion

The inclusion of dopants was found not to disrupt the final sintering density of the UO_2 fuel; however, distinct trends in microstructural evolution were observed. The incorporation of Mo and W, across all investigated concentrations, demonstrated limited solubility, resulting in a significant reduction in grain size, with final average grain sizes around 2–3 μm—below the acceptable range for commercial fuel specifications. This grain size reduction is attributed to secondary phase precipitates.

In contrast, Ni-doped UO_2 exhibited an inverse relationship between concentration and grain size. At concentrations up to 250–500 ppm, Ni appears to be soluble in the UO_2 matrix, as evidenced by progressive lattice contraction and moderate grain growth. The average grain sizes observed within this solubility range remained within the commercially acceptable range, suggesting that Ni, in controlled amounts, may offer an optimal balance: enhancing microstructural stability without drastically increasing self-diffusion. These properties make Ni a promising candidate for nuclear forensic tagging, as it can be effectively retained in the fuel while minimally impacting performance. However, Ni concentrations above ~500 ppm, along with all tested concentrations of Mo and W, appear to exceed their solubility limits in UO_2. This was evidenced by negligible changes in the UO_2 lattice parameter and a pronounced reduction in grain size, again likely due to the formation of secondary phases that limit grain

Acknowledgments

This work was supported by the U.S. Department of Energy, National Nuclear Security Administration, Office of Defense Nuclear Nonproliferation R&D

Reference

1. International Atomic Energy Agency.
2. Kristo, M. J., Robel, M., & Hutcheon, I. D. (2007). *Nuclear forensics and attribution for improved energy security: The use of taggants in nuclear fuel*. Lawrence Livermore National Laboratory.
3. Varga, Z., et al. (2022). Trends and perspectives in nuclear forensic science. *TrAC Trends in Analytical Chemistry, 146*, 116503.
4. Gooch, J., et al. (2016). Taggant materials in forensic science: A review. *TrAC Trends in Analytical Chemistry, 83*(Part B), 49–54.
5. Marks, N. E. C., Wellons, M., & Shields, A. E. (2024). An intentional nuclear forensics approach to support nuclear security: The use of taggants to support rapid provenance assessment. *International Conference on Nuclear Security*, Vienna, Austria.
6. Scott, S. M. M., et al. (2023). Intentional forensics: Tagging strategies for rapid nuclear material provenance assessment. *INMM & ESARDA Joint Annual Meeting*, Vienna, Austria.
7. Shollenberger, Q. R., et al. (2023). Molybdenum and tungsten isotope compositions of UO_2 fuel pellets: Implications for isotopically enriched taggants. *Journal of Nuclear Materials, 584*, 154583.
8. Wilson, B., et al. (2022). Irradiation of isotopically tagged UO_2 fuel for intentional forensics purposes. In *ANS Winter Meeting and Technology Expo 2022* (pp. 585–588). Transactions of the American Nuclear Society.
9. Hackenberg, R. E., et al. (2021). *Intentional uranium tagging for material provenance and pathway forensics (LA19-Intentional-Forensics-NDD3Bb): Annual report for FY21*. Los Alamos National Laboratory.
10. Ulrich, T. L., et al. (2025). Investigation of UO_2 doped with Fe_2O_3 sintered under a reducing atmosphere. *Journal of Nuclear Materials, 607*.
11. U.S. Nuclear Regulatory Commission. (n.d.). *Fuel fabrication*. https://www.nrc.gov/materials/fuel-cycle-fac/fuel-fab.html
12. World Nuclear Association. (2021). *Fuel fabrication*. https://world-nuclear.org/information-library/nuclear-fuel-cycle/conversion-enrichment-and-fabrication/fuel-fabrication
13. Crawford, D. C., Petti, D. A., & Pasamehmetoglu, K. (2007). An approach to fuel development and qualification. *Journal of Nuclear Materials, 371*, 232–242.
14. U.S. Nuclear Regulatory Commission. (2022). *Fuel qualification for advanced reactors* (NUREG-2246).
15. Cheniour, A., et al. (2023). Sensitivity of UO_2 fuel performance to microstructural evolutions driven by dilute additives. *Nuclear Engineering and Design, 410*, 112383.
16. Silva, C. M., Hunt, R. D., & Holliday, K. S. (2021). An evaluation of tri-valent oxide (Cr_2O_3) as a grain enlarging dopant for UO_2 nuclear fuels fabricated under reducing environment. *Journal of Nuclear Materials, 553*, 153053.

17. Scheele, R. D., Hanson, B. D., & Casella, A. M. (2021). Effect of added gadolinium oxide on the thermal air oxidation of uranium dioxide. *Journal of Nuclear Materials, 552*, 153008.
18. Zhong, Y., et al. (2021). Preparation and characterization of large grain UO_2 for accident tolerant fuel. *Frontiers in Materials, 8*, 651074.
19. Nikolopoulos, P., et al. (1977). Surface, grain boundary and interfacial energies in UO_2 and UO_2-Ni. *Journal of Nuclear Materials, 7*, 89–94.
20. Yao, T., et al. (2016). TiO_2 doped UO_2 fuels sintered by spark plasma sintering. *Journal of Nuclear Materials, 469*, 251–261.
21. Silva, C. M., Hunt, R. D., & Nelson, A. T. (2021). Microstructural and crystallographic effects of sol-gel synthesized Ti-doped UO_2 sintered under reducing conditions. *Journal of Nuclear Materials, 552*, 153003.
22. Terricabras, A. J., et al. (2024). Performance and properties evolution of near-term accident tolerant fuel: Cr-doped UO_2. *Journal of Nuclear Materials, 594*, 155022.
23. Arborelius, J., et al. (2006). Advanced doped UO_2 pellets in LWR applications. *Journal of Nuclear Science and Technology, 43*, 967–976.
24. ASTM International. (2016). *ASTM C753 − 16a Standard specification for nuclear-grade, sinterable uranium dioxide powder*.
25. Bergin, R., et al. (2024). Synthesis and characterization of isotopically barcoded nickel, molybdenum, and tungsten taggants for intentional nuclear forensics. *SSRN*.
26. Bergin, R., et al. (2025). Synthesis and characterization of isotopically barcoded nickel, molybdenum, and tungsten taggants for intentional nuclear forensics. *Talanta, 285*.
27. U.S. Nuclear Regulatory Commission. (2001). *SCDAP/RELAP5/MOD 3.3 Code Manual - MATPRO - A Library of Materials Properties for Light-Water-Reactor Accident Analysis* (NUREG/CR-6150, Vol. 4, Rev. 2).
28. ASTM International. (2020). *ASTM C1647-20: Standard practice for removal of uranium or plutonium, or both, for impurity assay in uranium or plutonium materials*.
29. ASTM International. (2012). *ASTM E112-12 Standard test methods for determining average grain size* (pp. 1–27).
30. Saville, A. I., et al. (2021). MAUD Rietveld refinement software for neutron diffraction texture studies of single- and dual-phase materials. *Integrating Materials and Manufacturing Innovation, 10*, 461–487.
31. Grazulis, S., et al. (2009). Crystallography Open Database: An open-access collection of crystal structures. *Journal of Applied Crystallography, 42*(4), 726–729.
32. Livneh, T. (2022). Resonant Raman scattering in UO_2 revisited. *Physical Review B, 105*, 045115.
33. Arborelius, J., et al. (2006). Advanced doped UO_2 pellets in LWR applications. *Journal of Nuclear Science and Technology, 43*(9), 967–976.
34. ASTM International. (n.d.). *Standard specification for sintered uranium dioxide pellets for light water reactors*.
35. Arborelius, J., et al. (2006). Advanced doped UO_2 pellets in LWR application. *Journal of Nuclear Science and Technology, 43*(9), 967–9761184.
36. Olds, T. A., et al. (2020). Oxidation and anion lattice defect signatures of hypostoichiometric lanthanide-doped UO_2. *Journal of Nuclear Materials, 530*, 151959.

37. He, H., & Shoesmith, D. (2010). Raman spectroscopic studies of defect structures and phase transition in hyper-stoichiometric UO_{2+x}. *Physical Chemistry Chemical Physics, 12*(28), 8109–8118.
38. Spano, T. L., et al. (2019). Comparative chemical and structural analyses of two uranium dioxide fuel pellets. *Journal of Nuclear Materials, 518*, 149–161.
39. Leenaers, A., et al. (2003). On the solubility of chromium sesquioxide in uranium dioxide fuel. *Journal of Nuclear Materials, 317*, 62–68.
40. Cooper, M. W. D., et al. (2018). The role of dopant charge state on defect chemistry and grain growth of doped UO_2. *Acta Materialia, 150*, 403–413.
41. Smith, H., et al. (2024). Fabrication, defect chemistry and microstructure of Mn-doped UO_2. *Scientific Reports, 14*, 1656.
42. Vazhappilly, T., & Pathak, A. K. (2019). Theoretical study on the mechanical and thermal properties of uranium dioxide doped with lanthanide fission products. *Journal of Nuclear Materials, 519*, 128–136.
43. Nicoll, S., et al. (1997). The behaviour of single atoms of molybdenum in urania. *Journal of Nuclear Materials, 240*, 185–195.
44. Kleykamp, H. (1985). The chemical state of the fission products in oxide fuels. *Journal of Nuclear Materials, 131*, 221–246.
45. Ha, Y.-K., et al. (2011). Behaviors of molybdenum in UO_2 fuel matrix. *Nuclear Engineering and Technology, 43*, 309–316.
46. Hollenbach, L. H., Jr. (2022). *Westinghouse Advanced Doped Pellet Technology (ADOPT™)* (WCAP-18482-NP-A).
47. Turnbull, J. A. (1973). The effect of grain size on the swelling and gas release properties of UO_2 during irradiation. *Journal of Nuclear Materials, 50*, 62–68.
48. Hilbert, R. F., et al. (1971). Mechanisms of swelling and gas release in uranium dioxide. *Journal of Nuclear Materials, 38*, 26–34.
49. Cooper, M. W. D., et al. (2018). The defect chemistry of $UO_{2\pm x}$ from atomistic simulations. *Journal of Nuclear Materials, 504*, 251–260.
50. Une, K., et al. (1993). Fission gas behavior during postirradiation annealing of large grained UO_2 fuels irradiated to 23 GWd/t. *Journal of Nuclear Science and Technology, 30*(3), 221–231.
51. McKinney, C., et al. (2023). Characterization of the radial microstructural evolution in LWR UO_2 using electron backscatter diffraction. *Journal of Nuclear Materials, 585*, 154605.
52. Wilson, B. A., et al. (2023). Nuclear fuel irradiation testbed for nuclear security applications. *Frontiers in Nuclear Engineering, 2*, 1123134.

APENDDIX A

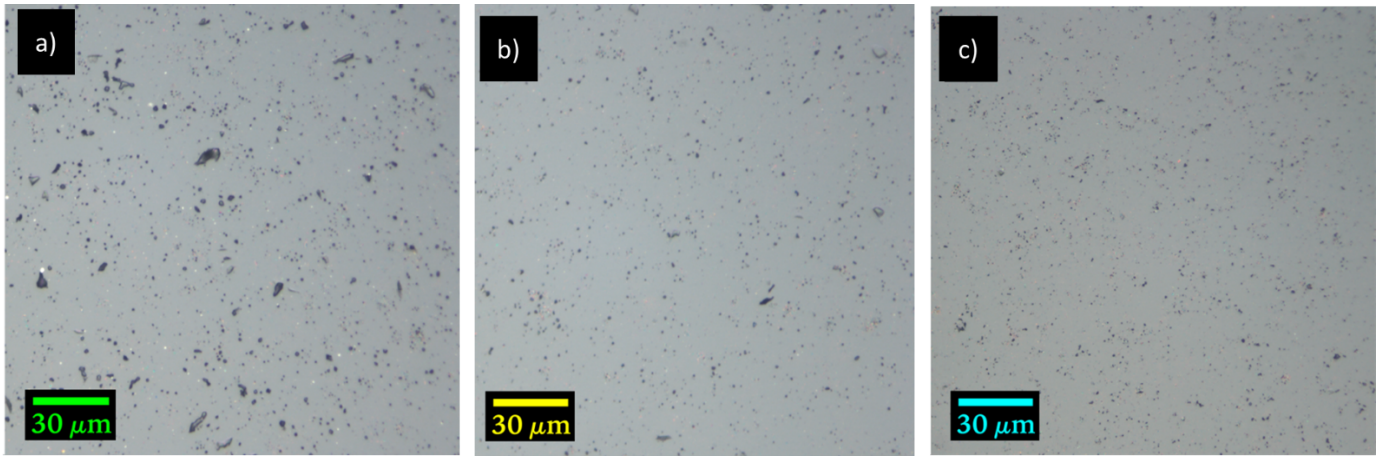

Figure A1: Optical microscopy images of UO_2 doped with 1000 ppm of (a) Ni, (b) Mo, and (c) W, showing the presence of precipitates (brigth sptos) in the microstructure.